Bioinspir. Biomim. **8** (2013) 016006 (13pp) doi:10.1088/1748-3182/8/1/016006

Bio-inspired aquatic robotics by untethered piezohydroelastic actuation

L Cen and A Erturk[1]

G W Woodruff School of Mechanical Engineering, Georgia Institute of Technology, Atlanta, GA 30332, USA

E-mail: alper.erturk@me.gatech.edu

Received 31 October 2012
Accepted for publication 2 January 2013
Published 24 January 2013
Online at stacks.iop.org/BB/8/016006

Abstract

This paper investigates fish-like aquatic robotics using flexible bimorphs made of macro-fiber composite (MFC) piezoelectric laminates for carangiform locomotion. In addition to noiseless and efficient actuation over a range of frequencies, geometric scalability, and simple design, bimorph propulsors made of MFCs offer a balance between the actuation force and velocity response for performance enhancement in bio-inspired swimming. The experimental component of the presented work focuses on the characterization of an elastically constrained MFC bimorph propulsor for thrust generation in quiescent water as well as the development of a robotic fish prototype combining a microcontroller and a printed-circuit-board amplifier to generate high actuation voltage for untethered locomotion. From the theoretical standpoint, a distributed-parameter electroelastic model including the hydrodynamic effects and actuator dynamics is coupled with the elongated-body theory for predicting the mean thrust in quiescent water. In-air and underwater experiments are performed to verify the incorporation of hydrodynamic effects in the linear actuation regime. For electroelastically nonlinear actuation levels, experimentally obtained underwater vibration response is coupled with the elongated-body theory to predict the thrust output. The measured mean thrust levels in quiescent water (on the order of ∼10 mN) compare favorably with thrust levels of biological fish. An untethered robotic fish prototype that employs a single bimorph fin (caudal fin) for straight swimming and turning motions is developed and tested in free locomotion. A swimming speed of 0.3 body-length/second (7.5 cm s^{-1} swimming speed for 24.3 cm body length) is achieved at 5 Hz for a non-optimized main body-propulsor bimorph combination under a moderate actuation voltage level.

(Some figures may appear in colour only in the online journal)

1. Introduction

Motor-based marine propulsion systems, such as screw propellers, can often be cumbersome and noisy as compared to numerous aquatic animals that have been optimized through the natural selection process for millions of years. The capacity of humankind to mimic these products of evolution at different geometric scales depends highly on the availability of suitable actuators. The motivation for fish-like biomimetic locomotion ranges from underwater sensing and exploration for sustainable ecology to drug delivery and disease screening in medicine [1–3]. Other than the use of conventional actuators, such as servomotors and hydraulic actuators employed in conjunction with various mechanisms [4–13], recently, various smart materials have been utilized for fish-like robotic fish development, such as ionic polymer–metal composites (IPMCs) [14–31], Shape memory alloys (SMAs) [32–37], magnetostrictive thin films [38–40], among other alternatives [41–43]. In particular, the IPMC technology [14–31] has received great interest for biomimetic locomotion primarily due to its low-voltage actuation and large-amplitude deflection capabilities. Conventional motor-based actuation involves

[1] Author to whom any correspondence should be addressed.

 © 2013 IOP Publishing Ltd Printed in the UK & the USA

complex structural design and provides high swimming speeds (per body length) whereas the use of smart materials enables the geometric scalability option along with simple design and noiseless performance at the expense of reduced swimming speeds (particularly in IPMCs due to low actuation forces).

Piezoelectric materials offer strong electromechanical coupling and actuation forces, high power density, and their fabrication methods at different scales are well established [44–47]. These materials exhibit the so-called direct and converse piezoelectric effects. The direct effect is the process of electric charge development in response to mechanical deformation, while the converse effect is the mechanical deformation resulting from an applied electric field in a piezoelectric material. From the standpoint of multifunctionality, the converse piezoelectric effect can be used for dynamic actuation in biomimetic locomotion over a range of frequencies, while the direct piezoelectric effect can be employed for harvesting [48] underwater energy toward enabling self-powered swimmer-sensor platforms [47]. Similar to IPMCs, the macro-fiber composite (MFC) piezoelectric actuators (developed at the NASA Langley Research Center in the last decade [49–51]) also exhibit high efficiency in size, reduced energy consumption, and noiseless performance. In addition, MFCs offer large dynamic stresses in bending actuation as well as high performance for both low-frequency and high-frequency applications. The MFC technology employs piezoelectric fibers of rectangular cross section along with interdigitated electrodes and leverages the 33-mode of piezoelectricity in bending actuation. With these characteristics, MFC-based robotic fish can provide both geometric scalability (as compared to motor-based robotic fish) and high performance swimming (as compared to IPMC-based robotic fish).

To the best of our knowledge, untethered (internally powered) piezoelectric robotic fish concept has not been covered in the literature [52–55]. High voltage input requirement and low strain output are the two disadvantages of piezoelectric transduction limiting the application of previously investigated piezoelectric structures for robotic fish development to use in free locomotion. In order to overcome the shortage of low strain in piezoelectric robotic configurations prior to the MFC technology, various kinematic magnification mechanisms were proposed by others [52–54]. However, the magnification component that is employed for creating larger vibration amplitudes typically creates energy loss and noise. As far as the high input voltage requirement is concerned, research groups have used tethered configurations to power piezoelectric robotic fish, which restricts the free-locomotion capability [52–55].

In this paper, fish-like aquatic robotics using MFC piezoelectric bimorphs is investigated theoretically and experimentally for carangiform locomotion [56]. First the in-air and underwater dynamics of an MFC bimorph cantilever are modeled for linear bending vibrations under dynamic piezoelectric actuation. The in-air electroelastic model is extended to obtain an underwater electrohydroelastic model accounting for the hydrodynamic effects following the work by Sader and co-workers [57–60] on atomic force microscopy cantilevers. Underwater dynamics of an elastically constrained bimorph propulsor is then coupled with Lighthill's elongated-body theory [61–64] to express the thrust output in quiescent water based on Lighthill's mean thrust expression. In-air and underwater experiments are conducted for model validation and for characterizing a bimorph propulsor. Finally, an untethered robotic fish prototype is developed and tested for straight swimming and turning motions in free locomotion.

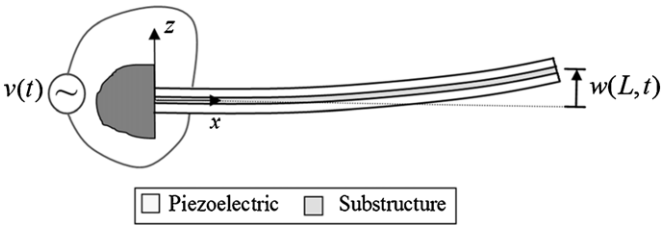

Figure 1. Schematic of a uniform cantilevered bimorph propulsor under dynamic voltage actuation to create bending vibrations (piezoelectric layers can be combined in series or in parallel).

2. Piezohydroelastic modeling of propulsor dynamics

2.1. In-air dynamics of a bimorph propulsor

The linear electroelastic equation of motion for in-air bending vibrations of a thin bimorph cantilever (figure 1) under dynamic voltage actuation is given by

$$D\frac{\partial^4 w(x,t)}{\partial x^4} + m\frac{\partial^2 w(x,t)}{\partial t^2} + c\frac{\partial w(x,t)}{\partial t} = \vartheta\left[\frac{\mathrm{d}\delta(x)}{\mathrm{d}x} - \frac{\mathrm{d}\delta(x-L)}{\mathrm{d}x}\right]v(t) \tag{1}$$

where D is the flexural rigidity of the composite cross section, m is the mass per length, c is the damping coefficient, ϑ is the electromechanical coupling term in the physical coordinates, $\delta(x)$ is the Dirac delta function, $v(t)$ is the actuation voltage, and $w(x,t)$ is the deflection of the reference surface in the transverse (z) direction at the longitudinal position x and time t. Here, m and c are altered for underwater vibrations due to the added mass and damping effects of hydrodynamic loads as discussed in section 2.2.

Separating the space- and time-domain variables and assuming single-mode (fundamental mode) response yields

$$w(x,t) \cong \phi(x)\eta(t) \tag{2}$$

where $\phi(x)$ and $\eta(t)$ are the mass-normalized eigenfunction and the modal coordinate of the fundamental transverse vibration mode for a clamped-free uniform beam. The mass-normalized eigenfunction for the first mode can be obtained as

$$\phi(x) = \sqrt{\frac{1}{mL}}\left[\cosh\frac{\lambda x}{L} - \cos\frac{\lambda x}{L} - \sigma\left(\sinh\frac{\lambda x}{L} - \sin\frac{\lambda x}{L}\right)\right] \tag{3}$$

and it satisfies the companion forms of the orthogonally conditions:

$$\int_0^L m\phi^2(x)\,\mathrm{d}x = 1, \quad \int_0^L \phi(x)D\frac{d^4\phi(x)}{\mathrm{d}x^4}\mathrm{d}x = \omega_{n,\mathrm{air}}^2 \tag{4}$$

Here, $\lambda = 1.875\,104\,07$, $\sigma = 0.734\,095\,514$, L is the length of the bimorph, and $\omega_{n,\text{air}}$ is the in-air natural frequency:

$$\omega_{n,\text{air}} = \lambda^2 \sqrt{\frac{D}{m_s L^4}} \tag{5}$$

where m_s is the structural mass per length.

For in-air vibrations, the mass per length in equation (1) is merely the structural mass per length:

$$m = m_s \tag{6}$$

while the in-air damping coefficient is

$$c = 2m_s\zeta_s\omega_{n,\text{air}} \tag{7}$$

where ζ_s is the in-air damping ratio which is assumed to be dominated by structural and other mechanical losses associated with in-air vibrations.

Following the standard analytical modal analysis procedure [65], i.e. substituting equation (2) into equation (1), multiplying the latter by the eigenfunction and integrating the resulting equation over the beam length, one obtains

$$\begin{aligned}\frac{d^2\eta(t)}{\mathrm{d}t^2}\int_0^L m\phi^2(x)\,\mathrm{d}x + \frac{\mathrm{d}\eta(t)}{\mathrm{d}t}\int_0^L c\phi^2(x)\,\mathrm{d}x + \eta(t)\\ \times \int_0^L \phi(x) D\frac{d^4\phi(x)}{\mathrm{d}x^4}\,\mathrm{d}x\\ = v(t)\int_0^L \phi(x)\vartheta\left[\frac{\mathrm{d}\delta(x)}{\mathrm{d}x} - \frac{\mathrm{d}\delta(x-L)}{\mathrm{d}x}\right]\mathrm{d}x\end{aligned} \tag{8}$$

yielding

$$\frac{d^2\eta(t)}{\mathrm{d}t^2} + 2\zeta_s\omega_{n,\text{air}}\frac{\mathrm{d}\eta(t)}{\mathrm{d}t} + \omega_{n,\text{air}}^2\eta(t) = \theta v(t) \tag{9}$$

where θ is the electromechanical coupling term in the modal coordinates:

$$\theta = \int_0^L \phi(x)\vartheta\left[\frac{\mathrm{d}\delta(x)}{\mathrm{d}x} - \frac{\mathrm{d}\delta(x-L)}{\mathrm{d}x}\right]\mathrm{d}x = \vartheta\frac{\mathrm{d}\phi(x)}{\mathrm{d}x}\bigg|_{x=L} \tag{10}$$

If the actuation voltage is assumed to be harmonic of the form

$$v(t) = V_0 \mathrm{e}^{j\omega t} \tag{11}$$

where V_0 is the actuation voltage amplitude, ω is the actuation frequency (in rad s^{-1}), and j is the unit imaginary number, then the steady-state response for the modal coordinate is

$$\eta(t) = \frac{\theta V_0 \mathrm{e}^{j\omega t}}{\omega_{n,\text{air}}^2 - \omega^2 + j2\zeta_s\omega_{n,\text{air}}\omega} \tag{12}$$

The resulting in-air tip velocity amplitude is therefore

$$\left|\frac{\partial w(L,t)}{\partial t}\right| \cong \left|\phi(L)\frac{\mathrm{d}\eta(t)}{\mathrm{d}t}\right| = \left|\frac{V_0\omega\theta\phi(L)}{\omega_{n,\text{air}}^2 - \omega^2 + j2\zeta_s\omega_{n,\text{air}}\omega}\right| \tag{13}$$

from which the tip velocity-to-actuation voltage frequency response function (FRF) can be extracted. It is important to note that this solution is valid for excitations around the fundamental natural frequency since higher vibration modes are not used in equation (2). In addition, the foregoing derivation neglects the geometric, material, and dissipative nonlinearities [66–68] and is strictly valid for linear vibrations only.

2.2. Underwater dynamics of a bimorph propulsor

In this section, hydrodynamic effects are included to predict the underwater vibrations of the cantilever based on the previous work by Sader *et al* [57–60] on atomic force microscopy cantilevers. Similar efforts are due to Brunetto *et al* [23], Mbemmo *et al* [24], and Aureli *et al* [28] for the underwater dynamics of IPMC propulsors. The following hydroelastic formulation [57–60] assumes geometrically small oscillations (relative to both length and width dimensions) of a uniform cantilever in unbounded fluid. Moreover, Sader's theory [57–60] assumes that the length-to-width ratio (L/b) is large and the accuracy of predictions decay as L and b become comparable.

The added mass per length m_a and the hydrodynamic damping ratio ζ_h can be expressed in terms of the hydrodynamic function Γ as [57]

$$m_a = \frac{\pi\rho_w b^2}{4}\Gamma_r \tag{14}$$

$$\zeta_h = \frac{1}{2Q_h} = \frac{\Gamma_i}{2\left(\frac{4m_s}{\pi\rho_w b^2} + \Gamma_r\right)} \tag{15}$$

where ρ_w is the mass density of water, Q_h is the quality factor due to hydrodynamic damping, Γ_r and Γ_i are the real and imaginary parts of hydrodynamic function Γ, respectively, and b is the width of the bimorph propulsor. The hydrodynamic function Γ can be calculated analytically or numerically. In this paper, we use the analytical $\Gamma(\text{Re})$ expression from Sader's work [57], which is a function of the Reynolds number (Re):

$$\Gamma(\text{Re}) = \Omega(\text{Re})\left[1 + \frac{4jK_1\left(-j\sqrt{j\,\text{Re}}\right)}{\sqrt{j\,\text{Re}}K_0\left(-j\sqrt{j\,\text{Re}}\right)}\right] \tag{16}$$

where K_0 and K_1 are the modified Bessel functions of the third kind and the Reynolds number (that uses the geometric scale b) is

$$\text{Re} = \frac{\rho_w\omega b^2}{4\mu} \tag{17}$$

where μ is the dynamic viscosity of water. In equation (16), $\Omega(Re)$ is the correction function to approximate the hydrodynamic function of rectangular beam from that of a circular cylinder [57]:

$$\Omega(\text{Re}) = \Omega_r(\text{Re}) + j\Omega_i(\text{Re}) \tag{18}$$

where

$$\begin{aligned}\Omega_r(\text{Re}) = (&0.913\,24 - 0.482\,74\psi + 0.468\,42\psi^2\\ &- 0.128\,86\psi^3 + 0.044\,055\psi^4 - 0.003\,5117\psi^5\\ &+ 0.000\,690\,85\psi^6) \times (1 - 0.569\,64\psi + 0.4869\psi^2\\ &- 0.134\,44\psi^3 + 0.045\,155\psi^4 - 0.003\,5862\psi^5\\ &+ 0.000\,690\,85\psi^6)^{-1}\end{aligned} \tag{19}$$

$$\begin{aligned}\Omega_i(\text{Re}) = (&-0.024\,134 - 0.029\,256\psi + 0.016\,294\psi^2\\ &- 0.000\,109\,61\psi^3 + 0.000\,064\,577\psi^4 - 0.000\,044\,51\psi^5)\\ &\times(1 - 0.597\,02\psi + 0.551\,82\psi^2 - 0.183\,57\psi^3\\ &+ 0.079\,156\psi^4 - 0.014\,369\psi^5 + 0.002\,8361\psi^6)^{-1},\end{aligned} \tag{20}$$

and $\psi = \log_{10} \mathrm{Re}$. According to Sader [57], equation (16) is accurate to within 0.1 % over the range $10^{-6} \leqslant \mathrm{Re} \leqslant 10^{4}$ for both real and imaginary parts. Simplified expressions of the hydrodynamic function Γ are also available depending on the range of the Reynolds number [69, 70]. Although the present discussion is given for small oscillations, we note that particularly hydroelastic nonlinearities can easily be pronounced depending on the aspect ratio, requiring correction of the hydrodynamic function [70, 71].

As far as the dissipation mechanisms are concerned, both structural and hydrodynamic damping effects are taken into account for the total damping ratio (ζ_w) of underwater vibrations:

$$\zeta_w = \zeta_s + \zeta_h \tag{21}$$

The mass per length and damping coefficient terms in equation (1) for underwater vibrations are

$$m = m_w = m_s + m_a \tag{22}$$

$$c = 2m\zeta_w\omega_{n,\mathrm{water}} = 2m_w(\zeta_s + \zeta_h)\omega_{n,\mathrm{water}} \tag{23}$$

and the mass-normalized eigenfunction in equation (2) satisfies

$$\int_0^L m\phi^2(x)\,\mathrm{d}x = 1, \quad \int_0^L \phi(x)D\frac{d^4\phi(x)}{\mathrm{d}x^4}\,\mathrm{d}x = \omega_{n,\mathrm{water}}^2 \tag{24}$$

Since the underwater mass per length is due to equation (22), the underwater natural frequency $\omega_{n,\mathrm{water}}$ is obtained from the in-air natural frequency $\omega_{n,\mathrm{air}}$ (which is approximately the in-air resonance frequency for $\zeta_s \ll 1$) through Chu's formula [72] modified by the real part of the hydrodynamic function Γ_r [57]:

$$\omega_{n,\mathrm{water}} = \omega_{n,\mathrm{air}}\sqrt{\left(1 + \frac{\pi\rho_w b^2}{4m_s}\Gamma_r\right)^{-1}} \tag{25}$$

where $\omega_{n,\mathrm{air}}$ is given by equation (5).

The resulting underwater tip velocity response amplitude is therefore

$$\left|\frac{\partial w(L,t)}{\partial t}\right| \cong \left|\phi(L)\frac{\mathrm{d}\eta(t)}{\mathrm{d}t}\right| = \left|\frac{V_0\omega\theta\phi(L)}{\omega_{n,\mathrm{water}}^2 - \omega^2 + j2\zeta_w\omega_{n,\mathrm{water}}\omega}\right| \tag{26}$$

where θ is given in equation (10). However, the eigenfuction $\phi(x)$ in equations (10) and (26) is normalized according to equation (24) with m given by equation (22), i.e. the mass term in equation (3) is due to equation (22) for underwater vibrations.

2.3. Hydrodynamic mean thrust in terms of the underwater velocity response

A thrust estimation model that couples the actuator dynamics and hydrodynamic effects is essential to predict the piezohydroelastic response of bio-inspired robotic fish and to further optimize as well as control the resulting system dynamics. Two main methods have been widely used in thrust calculation for robotic fish [18, 27, 28, 39, 40, 56]. One of these methods is Taylor's *resistive* method [73, 74]. In this approach, the mean thrust is estimated from the total drag force, which often necessitates the identification of the drag coefficient for the fish body. The second widely employed approach is the *reactive* method that employs Lighthill's elongated-body theory [61–64], which is based on the slender-body theory of aerodynamics. The reactive method, or the elongated-body theory, is based on the reactive forces between the 'virtual mass' of water and the swimmer body. The reactive method is more suitable to use with high Reynolds numbers while the resistive method is applicable to the cases of low Reynolds numbers. Evidently the ideal modeling approach would be a combination of resistive and reactive effects to account for all locomotion patterns [56] and values of Reynolds numbers. Nevertheless, as pointed out by Lighthill [64], the reactive forces are known to dominate the carangiform motion [56] (that is similar to the motion pattern in this work), hence we focus on the use of reactive method for thrust estimation.

In most cases of robotic fish thrust estimation [27, 28, 38–40], it becomes necessary to identify certain calibration factors, such as the drag coefficient, which removes the possibility of obtaining an *a priori* estimate of the thrust resultant solely from the underwater vibration response. Lighthill's elongated-body theory was used in previous IPMC-based robotic fish studies to predict the steady-state cruising speed [24, 27] by equating the thrust expressions from the reactive and resistive methods, where the drag coefficient was measured by spring scales while pulling the fish with different velocities.

In the present work, Lighthill's theory [61–64] is employed alone to estimate the mean thrust in quiescent water as a first approximation. The mean thrust (T) in Lighthill's theory is given in the presence of an external relative free stream of speed U (which is essentially the swimming speed) as

$$T = \frac{1}{2}m_v\left[\overline{\left(\frac{\partial w}{\partial t}\right)^2} - U^2\overline{\left(\frac{\partial w}{\partial x}\right)^2}\right]_{x=L} \tag{27}$$

where the over-bar stands for the mean value and m_v is the virtual mass density at $x = L$, expressed as

$$m_v = \frac{\pi\rho_w b^2}{4}\beta \tag{28}$$

Here, β is a virtual mass coefficient that is close to unity [63] for the wavelength and body length considered in the experimental section of this work (hence $\beta \cong 1$).

In equation (27), we set $U \to 0$ to approximate quiescent water condition:

$$T \cong \frac{1}{2}m_v\left.\overline{\left(\frac{\partial w}{\partial t}\right)^2}\right|_{x=L} = \frac{\pi\rho_w b^2}{8}\overline{\left(\frac{\partial w(L,t)}{\partial t}\right)^2} \tag{29}$$

where the mean thrust T depends only on the tip velocity and the virtual mass for quiescent water approximation.

3. Details of the experimental setup and calibration

3.1. Setup for in-air tip velocity FRF measurements

The MFC bimorph tested and characterized in the experiments is shown in figure 2 along with its clamp and fixture employed for the in-air actuation FRF measurements. The bimorph is made of two custom-made hydrophobic M8528-P1 (Smart

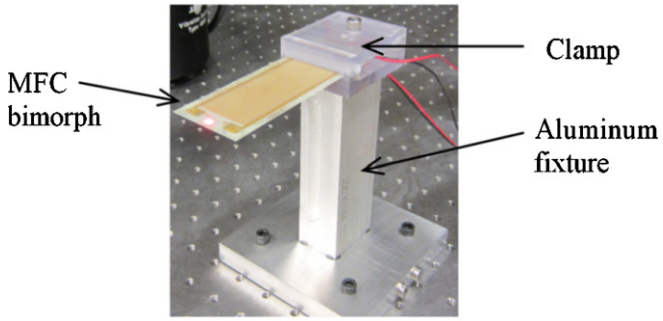

Figure 2. In-air configuration of the bimorph MFC cantilever for the measurement of its tip velocity-to-actuation voltage FRF.

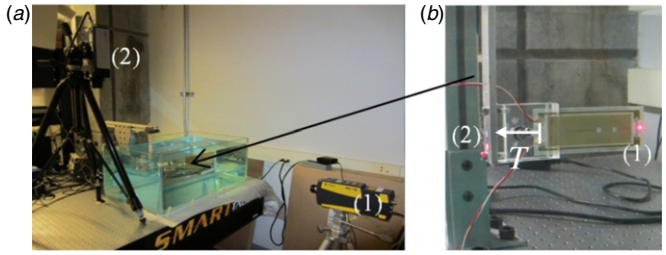

Figure 3. (*a*) Experimental setup used for thrust measurement of a bimorph propulsor in quiescent water: laser (1) measures the transverse tip velocity while laser (2) measures the elastically constrained head displacement through a 45° mirror; (*b*) close-up view showing the measurement points of lasers (1) and (2) on the MFC bimorph propulsor.

Table 1. Geometric and structural properties of the bimorph (*L*: overhang length; *b*: total width; *h*: total thickness; *D*: flexural rigidity; m_s: structural mass per length).

L (mm)	b (mm)	h (mm)	D (N m^2)	m_s (kg m^{-1})
90.2	35.0	0.67	0.0171	0.065

Material Corp.) MFC laminates with no separate substructure layer other than the Kapton and epoxy layers of the MFCs. A vacuum bonding process is employed by using high shear strength epoxy to assemble the piezoelectric laminates (this process is described elsewhere [75]). The basic geometric and structural properties of the bimorph are given in table 1. The electrode leads of the two MFCs are combined in parallel throughout the experiments discussed in this paper. A vertically aligned laser vibrometer is used along with the monitored actuation signal in order to obtain the transverse (vertical direction in figure 2) tip velocity-to-actuation voltage FRFs of the MFC bimorph in air.

3.2. Setup for underwater tip velocity FRF and mean thrust measurements

The experimental setup used for the underwater tip velocity and thrust measurements is shown in figure 3(*a*). As shown in figure 3(*b*), the MFC bimorph is fixed with the same clamp in the underwater experiments. Laser (1) measures the transverse tip velocity under dynamic actuation while laser (2) measures the head displacement (constrained by an aluminum cantilever) through a small mirror that makes a 45° angle with

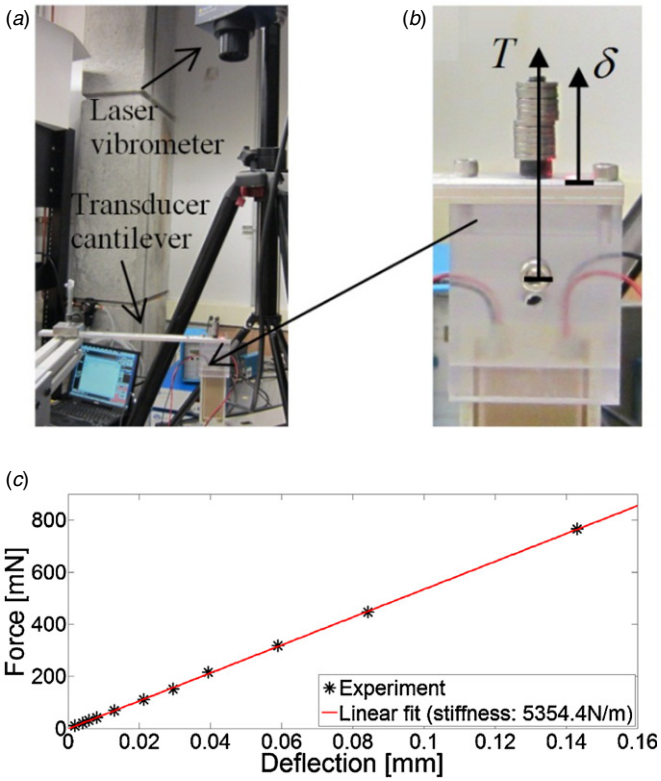

Figure 4. (*a*) Setup used for the thrust-displacement calibration experiment with the MFC bimorph, its clamp, and the transducer cantilever; (*b*) close-up view showing the point of applied loads at the center of MFC bimorph and the deflection measurement point; (*c*) linear calibration curve with the calculated linear stiffness (T/δ)value.

the horizontal plane. The elastically constrained mean head displacement is correlated to the mean thrust as described in the next section. Note that both laser signals (velocity and displacement) are divided by the refractive index of water ($n = 1.333$) in the underwater experiments [47]. Attention is also given to avoid the capturing of undesired interface (aquarium glass) reflection by slightly tilting the laser sensor head.

3.3. Calibration of the thrust measurement setup

The setup employed for mean thrust measurement is similar to the one used by Erturk and Delporte [47]. The MFC bimorph and its clamp are fixed at the tip of a horizontally located aluminum beam which functions as a *transducer cantilever* along with a vertically pointing laser vibrometer used in the displacement measurement mode (figure 4(*a*)). This laser vibrometer employed for measuring the head displacement corresponds to laser (2) in the underwater experiments (figure 3(*a*)). The purpose of the in-air setup shown in figure 4(*a*) is to relate the thrust caused by actuation in the underwater experiments to the deflection of the aluminum transducer cantilever.

It is assumed that the mean thrust resultant (T) of the bimorph propulsor (in the underwater experiments) acts through the center of its head, causing the deflection of δ at the location of the reflector for laser (2) in the underwater arrangement given by figure 3(*a*). Different values of small

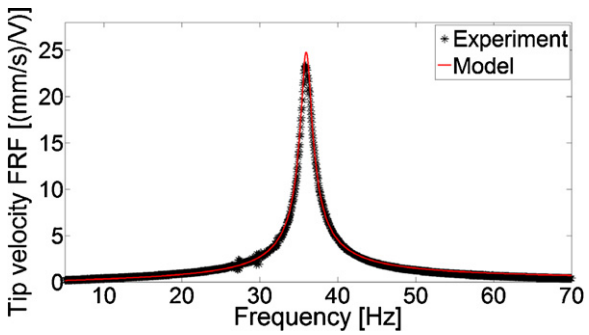

Figure 5. Measured and calculated in-air tip velocity-to-actuation voltage FRFs of the MFC bimorph in its linear actuation regime.

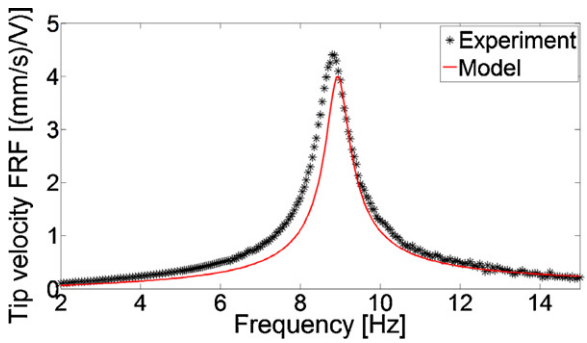

Figure 6. Measured and calculated underwater tip velocity-to-actuation voltage FRFs of the MFC bimorph in its linear actuation regime.

masses are gradually located at the center of the top surface to emulate the mean thrust (figure 4(*b*). The vertically pointing laser measures the resulting deflection at the reflector, which is employed to obtain the thrust-displacement calibration line shown in figure 4(*c*).

It is important to note that the underwater fundamental resonance frequency of the aluminum transducer cantilever (in the presence of the MFC bimorph) is sufficiently higher than the underwater actuation frequencies of interest, which is checked by impact hammer testing (not discussed here). Moreover, the hydrostatic pressure effects are assumed to cancel out, leaving only the hydrodynamic resultant. Therefore, in the underwater experiments, the tip deflection of the transducer cantilever is mainly due to the dynamics of the MFC bimorph propulsor so that the elastically constrained mean head displacement value can be employed to calculate the mean thrust based on the in-air calibration.

4. Experiments and model validation

4.1. In-air tip velocity FRF and parameter identification

Low-voltage harmonic input is applied to the MFC bimorph for the frequency range of 5–70 Hz with an increment of 0.05 Hz. Figure 5 exhibits the experimentally measured tip velocity-to-actuation voltage FRF and the model prediction using equation (13) for the linear actuation regime of the bimorph. The fundamental in-air resonance frequency is 35.5 Hz. The in-air damping ratio (attributed mostly to structural losses for small oscillations) is identified as $\zeta_s = 0.02$ while the identified electromechanical coupling in the physical coordinates (see equation (1)) is $\vartheta = 23.03\mu\,\mathrm{NmV}^{-1}$. The modal electromechanical coupling that depends on the in-air eigenfunction due to equation (10) is $\theta = 8.878 \times 10^{-3}\ \mathrm{N\ (V\ kg^{-1/2})^{-1}}$.

4.2. Underwater tip velocity FRF

The MFC bimorph is submerged in water (as depicted in figure 3) along with its clamp and aluminum fixture used in thrust calibration (figure 4). Low-voltage harmonic actuation is applied to the MFC bimorph for the frequency range of 2–15 Hz with an increment of 0.05 Hz. The fundamental underwater resonance frequency of linear vibrations is measured as 8.7 Hz. According to equation (21), the total underwater damping ratio is due to the structural and hydrodynamic damping effects. Equations (15) and (17) yield $\zeta_h = 0.0119$ and Re $\cong$ 19430, and eventually, from equation (21), one obtains $\zeta_w = 0.0319$. The electromechanical coupling in the physical coordinates is the same as the one obtained from in-air vibration test ($\vartheta = 23.03\mu\,\mathrm{NmV}^{-1}$) while the modal electromechanical coupling becomes $\theta = 2.325 \times 10^{-3}\ \mathrm{N\ (V\ kg^{-1/2})^{-1}}$ due to equation (10) in which the eigenfunction is normalized according to equation (24) by using the underwater mass per length given by equation (22). Therefore, one can predict the underwater tip velocity FRF using equation (26) as shown in figure 6.

The agreement between the experimental measurement and theoretical prediction is good in the linear actuation regime of the bimorph. Equation (25) predicts the underwater resonance frequency as 8.8 Hz with an error of 1.1% relative to the experimental value (8.7 Hz). Both the total underwater damping and natural frequency are predicted in terms of the in-air dynamics and fluid properties with good accuracy. Expectedly the linear model predictions would fail under high actuation voltage levels due to geometric and electroelastic nonlinearities [66–68]. Nonlinear modeling of MFC dynamics under high voltage actuation and incorporation of nonlinear hydrodynamic effects [70, 71] in such a nonlinear model are of interest for future work.

4.3. Mean thrust and tip velocity correlation for different actuation voltage levels

The frequency range covered in the underwater thrust measurements is 0.5–15 Hz with a fine increment of 0.25 Hz in the 6–8 Hz range (resonance region) and a relatively coarse increment of 0.5 Hz outside the resonance region. Three time-domain head displacement measurements are taken at each frequency (pre-actuation, actuation, and post-actuation [47]) while the tip velocity in the transverse direction is measured simultaneously. The reference point is calculated as the average of the pre-actuation and post-actuation values. Based on the previously discussed calibration (section 3.3), the mean thrust is a linear function of the mean displacement of the aluminum cantilever. This mean displacement is the difference between the mean values of the *actuation*

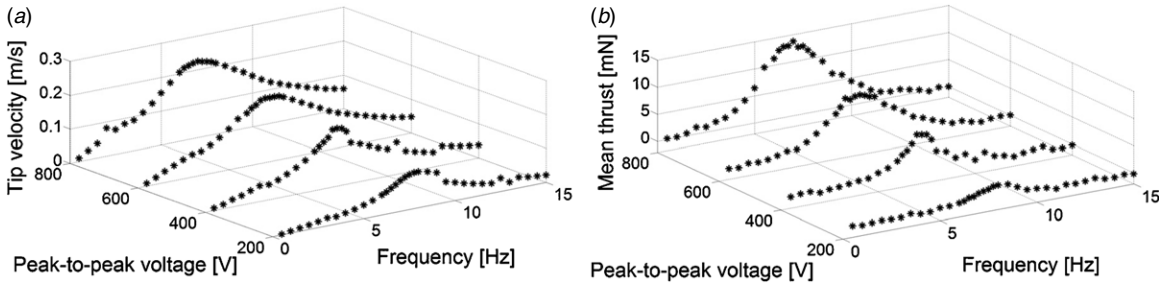

Figure 7. Experimental (*a*) tip velocity and (*b*) mean thrust curves for four different peak-to-peak voltage levels: 200, 400, 600, and 800 V.

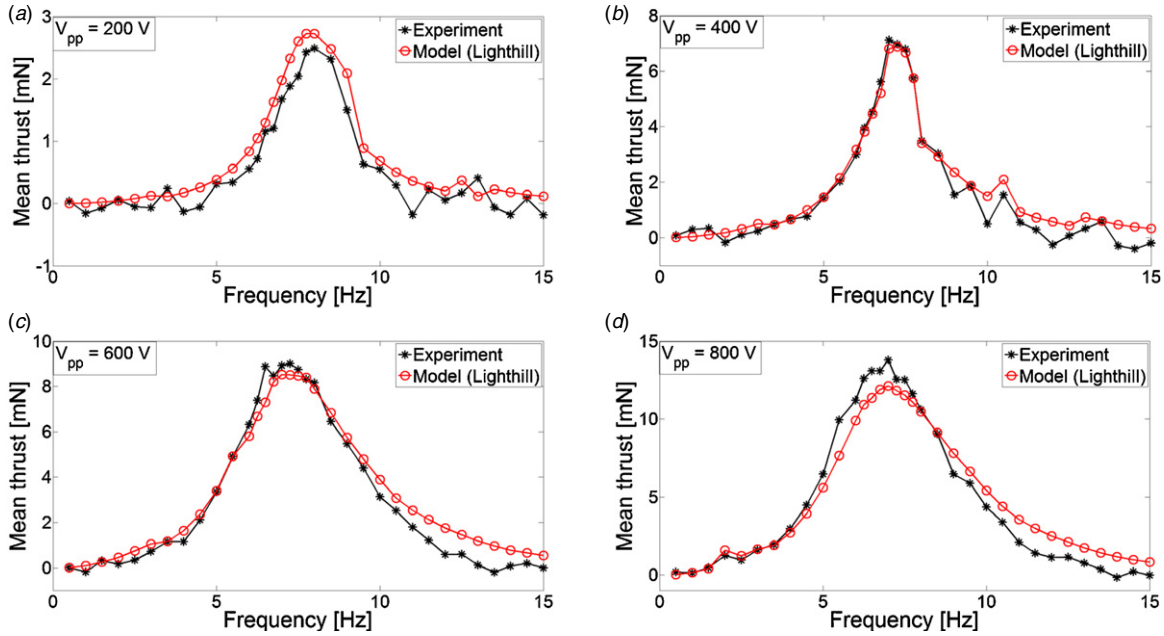

Figure 8. Measured and predicted thrust curves for the peak-to-peak voltage inputs of (*a*) 200, (*b*) 400, (*c*) 600, and (*d*) 800 V.

displacement and the *reference* point. From this mean displacement, the mean thrust is extracted using the linear calibration curve in figure 4(*c*).

The experimental tip velocity and mean thrust measurements for the peak-to-peak actuation voltage levels of 200, 400, 600, and 800 V are shown in figures 7(*a*) and (*b*), respectively. Clearly, there is a direct correlation between these two independent measurements since the thrust level increases with increasing tip velocity. It should be noted that these high actuation voltage levels fall into the nonlinear regime due to the electroelastic, geometric, and dissipative nonlinear effects. The softening nonlinearity (resulting in the shifting of the resonance frequency to the left) with increased actuation input is a typical behavior of piezoelectric cantilevers under high voltage actuation [67].

Using equation (29) resulting from Lighthill's theory for quiescent water condition, one can estimate the thrust curves in terms of the virtual mass and measured tip velocity. These predictions are shown in figures 8(*a*)–(*d*) for four different actuation voltage levels. Note that, particularly in figure 8(*a*) (which is the lowest voltage case among these four measurement sets), the frequencies away from the resonance region are prone to noise effects in the measurements due to low thrust resultant (caused by low

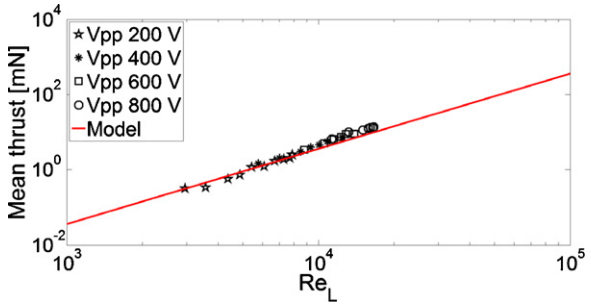

Figure 9. Experimental and theoretical mean thrust versus the modified Reynolds number. The experimental data belongs to four different actuation voltage levels and different frequencies around the fundamental resonance.

displacement). Based on figures 8(*a*)–(*d*), it can be concluded that the reduced form of Lighthill's theory [62–64] for quiescent water can predict the mean thrust in terms of the tip velocity with good accuracy. One should recall that figures 8 and 9 are electroelastically nonlinear, and therefore the linear derivations given in sections 2.1 and 2.2 do not intent to predict these dynamics quantitatively. However, Lighthill's formula reduced for quiescent water in section 2.3 does correlate the tip velocity to mean thrust with good accuracy in figure 8.

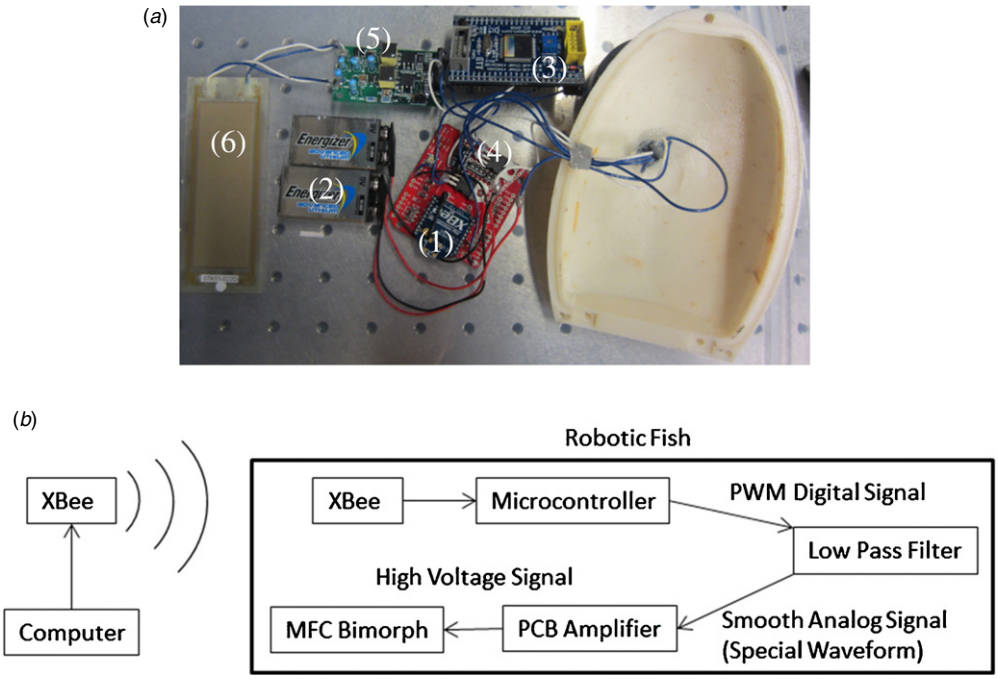

Figure 10. (*a*) Components for the untethered piezoelectric robotic fish system: (1) XBee radio; (2) 9 V batteries; (3) microcontroller; (4) low pass filter and voltage regulators; (5) voltage amplifier; (6) MFC bimorph; and (*b*) electronic schematic of the robotic fish system.

4.4. Identification of the thrust coefficient

In this section, the hydrodynamic thrust coefficient of the propulsor is extracted based on the mean thrust and transverse tip velocity of the piezoelectric propulsor. This process is analogous to the thrust coefficient identification procedure given in [76], that employed computational fluid dynamic simulations for an IPMC propulsor. First we define the modified Reynolds number as

$$\mathrm{Re}_L = \frac{\omega \gamma L}{\upsilon} \tag{30}$$

where $\gamma = |w(L,t)|$ is the tip displacement amplitude at frequency ω while υ is the kinematic viscosity of water ($\upsilon = \mu/\rho_w$). It is useful to compare equation (30) with equation (17) and note that the modified Reynolds number introduced at this point uses the total length and the underwater vibration response as the geometric scale.

The thrust coefficient C_τ is defined as [76]

$$C_\tau = \frac{\tau}{\frac{1}{2}\rho_w \omega^2 \gamma^2 L} \tag{31}$$

where τ is the thrust per unit width ($\tau = T/b$) and we note from equations (30) and (31) that $\tau \propto \mathrm{Re}_L^2$.

Substituting equation (29) into equation (31) gives

$$C_\tau = \frac{\frac{\pi \rho_w b}{8}\overline{\left(\frac{\partial w(L,t)}{\partial t}\right)^2}}{\frac{1}{2}\rho_w \omega^2 \gamma^2 L} = \frac{\frac{\pi \rho_w b}{8}\frac{\omega^2\gamma^2}{2}}{\frac{1}{2}\rho_w \omega^2 \gamma^2 L} = \frac{\pi b}{8L} \cong 0.1524. \tag{32}$$

Another manipulation of equations (30) and (31) provides the variation of the mean thrust with modified Reynolds number as

$$T = \frac{\pi \rho_w b^2 \upsilon^2}{16 L^2}\mathrm{Re}_L^2 \cong 3.322 \times 10^{-11}\mathrm{Re}_L^2 \ \text{[in Newtons]} \tag{33}$$

which is a very useful expression to correlate the modified Reynolds number to mean thrust.

Figure 9 displays the variation of the mean thrust with modified Reynolds number based on the experimental thrust measurements at different actuation voltage levels and frequencies along with the prediction of equation (33) in log–log scale. The proportionality between mean thrust T and Re_L^2 is observed in the experimental data and is well predicted by the modeling approach based on Lighthill's theory.

5. Prototype for untethered locomotion

5.1. Electronic architecture for untethered swimming

Despite the advantages of MFCs due to large dynamic actuation stresses, structural flexibility, silent operation, and wide frequency range of effective performance, the requirement of high voltage input limits its application in free (untethered) locomotion for robotic fish development. In this section, a printed-circuit-board (PCB) high-voltage amplifier is implemented along with a microcontroller to overcome this issue in free locomotion. To our knowledge, this section presents the first untethered piezoelectric robotic fish since the configurations in previous efforts [52–55] were actuated by external power through tethers.

A separate bimorph propulsor is fabricated for the free-locomotion experiments. An embedded power and actuation system is designed for this prototype, which can generate high input voltage for the MFC bimorph propulsor. As shown in figure 10(*a*), this system consists of two 9 V batteries, a microcontroller (ATmega 128), a wireless device (XBee 1mW Wire Antenna—Series 1 (802.15.4)) and a PCB amplifier (AMD2012-CE3) specially designed for the MFC actuator

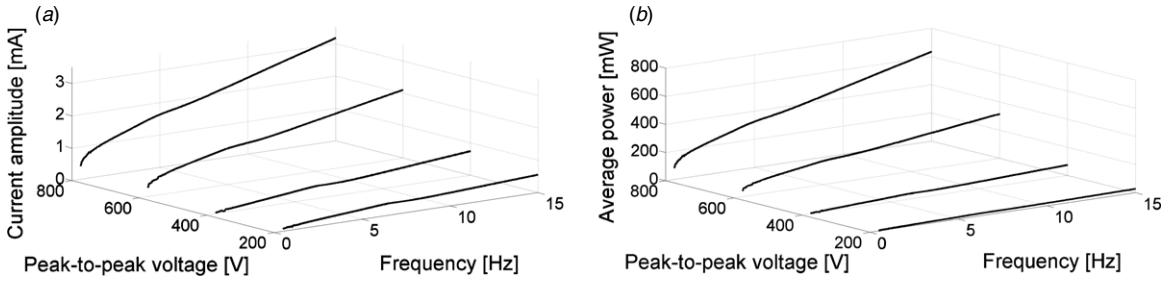

Figure 11. Experimental (*a*) current amplitude and (*b*) average power curves of the MFC bimorph under four different peak-to-peak voltage levels: 200 V, 400 V, 600 V, and 800 V.

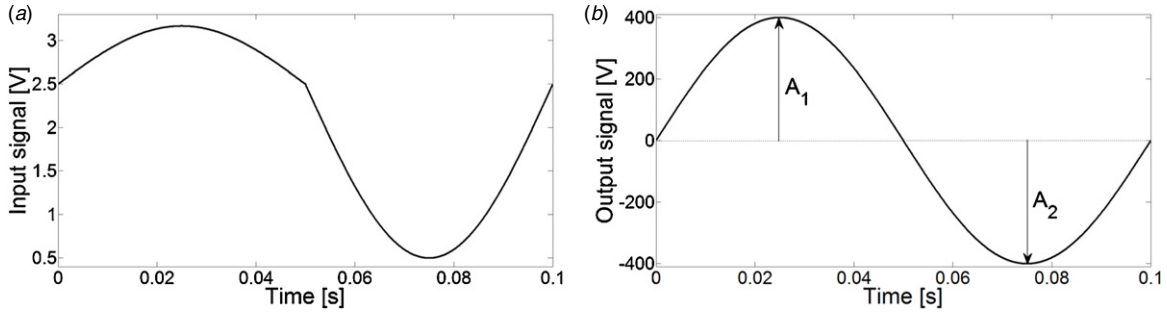

Figure 12. (*a*) Input and (*b*) output signals of the PCB amplifier to generate a sinusoidal peak-to-peak actuation voltage of 800 V at 10 Hz. The microcontroller can provide signal inputs to PCB amplifier to create oscillatory actuation voltage signals with $A_1 \neq A_2$ for turning motion.

(Smart Material Corp.). In order to obtain smooth sinusoidal voltage for the MFC bimorph, a low pass filter is added to filter out the high frequency noise from the pulse width modulation (PWM) signals. The detailed schematic of the actuation system is shown in figure 10(*b*).

5.2. Power consumption analysis

In order to enable untethered locomotion of the MFC-based robotic fish, a portable power system has to be designed to generate the high voltage for MFC bimorph actuation. The maximum output voltage level for the microcontroller is around 5 V, which is much lower than the requirements for MFC actuation. A specifically designed PCB amplifier (AMD2012-CE3) is utilized in the power system, which is able to generate high voltage from −500 to 1500 V according to the control input signal from 0 to 5 V. This PCB amplifier requires only 12 V input voltage supply. Therefore, one can build the mobile power system by simply using two 9 V batteries, the microcontroller, the PCB amplifier and the corresponding voltage regulators, as shown in figure 10(*a*). These two 9 V batteries can support the continuous operation of the system for about 30 min. The power consumption of the overall electronic system is around 3–5 W.

The current amplitude and average power plots for the MFC bimorph at different frequencies and actuation voltages are shown in figure 11. Figure 11(*b*) shows that the average power input to the MFC bimorph around its fundamental mode is less than 0.5 W (for the sinusoidal peak-to-peak voltage of 800 V). It should be noted that the results in figure 11(*b*) is an overestimation as far as the truly consumed power is concerned since these modulus curves include not only resistive but also reactive power. The overall power consumption of the robotic fish can therefore be further reduced by optimizing the actuation circuit design in the future.

5.3. Microcontroller, PCB voltage amplifier, and wireless control

In order to provide sinusoidal high voltage for the MFC bimorph, the microcontroller is programmed to generate a special waveform by PWM. Specifically, 0 V input signal generates −500 V output; 2.5 V input signal generates 0 V output; 5 V input signal generates 1500 V output. These values are the voltage limits of MFCs without depolarization. An example is given in figure 12 for the case of generating a sinusoidal peak-to-peak voltage of 800 V at 10 Hz using the PCB amplifier.

The microcontroller is able to generate various waveforms by its PWM function and the power system can provide the high voltage sinusoidal output (up to 2000 V peak-to-peak) for the MFC bimorph propulsor. The frequency, mean voltage, and amplitudes of the PCB amplifier output signal can be controlled by adjusting the rate and duty cycle of the PWM signals. The swimming speed is easily controlled through the PCB amplifier output signal frequencies and amplitudes. In addition, turning speed and direction are controlled by setting different values for the amplitudes A_1 and A_2 shown in figure 12(*b*).

Wireless control is performed through serial communication. Commands are sent by a laptop computer through a USB connected XBee Explorer. An XBee module inside the robotic fish body receives the commands and transfers them to the microcontroller, which can change the PWM waveform. Therefore, wireless communication controls the swimming speed of the robotic fish by setting the rate and duty cycle of

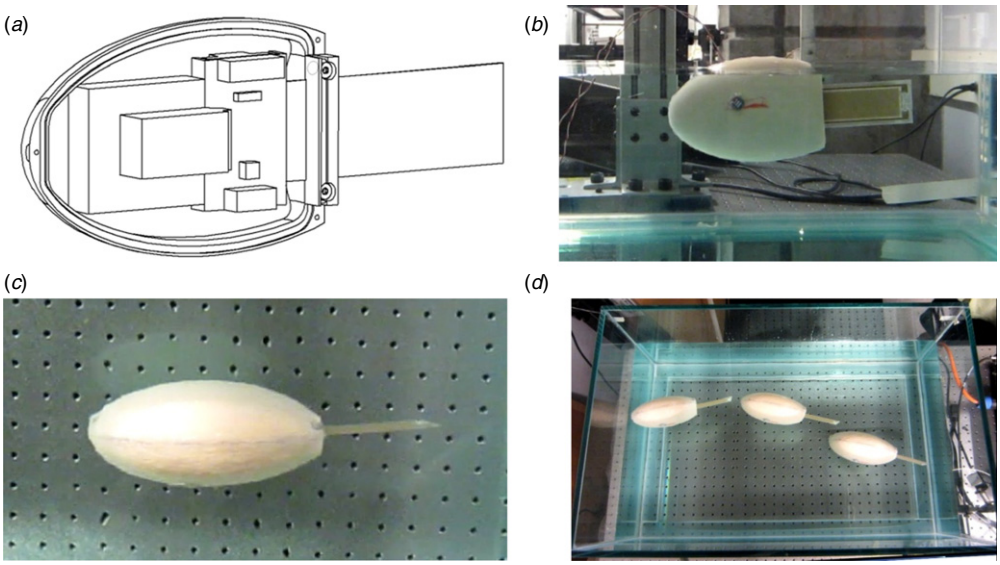

Figure 13. Untethered robotic fish prototype for free locomotion in (*a*) modeled view; (*b*) side view; (*c*) top view; and (*d*) combined motion capture involving turning motion. Swimming speed under peak-to-peak actuation voltage of 1000 V at 5 Hz is approximately 7.5 cm s^{-1}.

Table 2. Components of the piezoelectric robotic fish prototype (units are in grams).

MFC bimorph		11
Power, wireless and actuation system	Two batteries	64.8
	Microcontroller	18
	PCB amplifier	13.4
	XBee module	16.9
	Battery connectors	4
	Two voltage regulators	3.6
	Capacitor	1
	Wires	6
	Switch	0.8
Robotic fish body (shell, clamp, glue, and waterproof tapes, etc)		168.8
Counter weight		233.5
Total mass of the robotic fish		541.8

the PWM, which affect the vibration frequency and amplitude of the MFC propulsor. The Xbee signal would penetrate the water just a few centimeters so the robotic fish is tested close to surface. The wireless communication is used for testing the change of speed and direction during swimming.

5.4. Fabricated prototype and free locomotion tests

The modeled view and pictures of the robotic fish prototype are shown in figure 13. The fish body is designed to provide a waterproof enclosure for the electronics components and is realized using a fused deposition modeling machine. This creates an Acrylonitrile Butadiene Styrene plastic shell, that when printed is buoyant in water. An O-ring was integrated into the rim to ensure the interior of the fish stayed dry in order to protect the electronics. This prototype is intended merely for proof of concept, as the non-optimized volume (and hence buoyant force) requires a significant amount of counterweight. The total weight of the prototype is 541.8 grams, as given in the detailed mass analysis in table 2.

The swimming speed for a peak-to-peak actuation voltage of 1000 V at 5 Hz is measured as 7.5 cm s^{-1}.[2] This is equivalent to almost 0.3 body length per second and it compares favorably with several smart actuator-based aquatic robots reported in the literature (including tethered ones) [3][3] even though the present prototype excludes the additional passive caudal fin extension and volumetric optimization. The passive caudal fin extension is known to improve not only the thrust amplitude but also the bandwidth of effective excitation frequencies as shown by Erturk and Delporte [47]. Further improvements can be made by increasing the actuation voltage to a larger level with a dc offset (since MFC laminates have asymmetric voltage limits: −500 to 1500 V).

Table 3 and figure 14 present the performance comparison of the current non-optimized prototype with other untethered smart material-based and motor-based untethered robotic fish from the literature (these data should be considered as typical—not necessarily optimal—performance results). The performance metric is taken as the swimming speed per body length. Motor-based robotic fish generally has larger speed per body length than smart material-based counterparts whereas the latter offers ease of fabrication and geometric scalability. According to figure 14, the preliminary robotic fish presented in this work is near the intersection of smart material-based and motor-based robotic fish. Therefore MFC-based robotic fish provides geometric scalability (as compared to motor-based robotic fish) and high performance swimming (as compared to IPMC-based robotic fish).

[2] The boundary conditions in free locomotion are no longer exactly clamped-free due to the electronic hardware attachment at the head with finite translational and rotational inertia (which can be accounted for in structural dynamic modeling). Therefore the fundamental resonance frequency of the robotic fish configuration (figure 13) does not correspond to the resonance frequency of the clamped-free case (figure 3).

[3] Note that the piezoelectric-based robot [53] reviewed by Chu *et al* [3] was tethered.

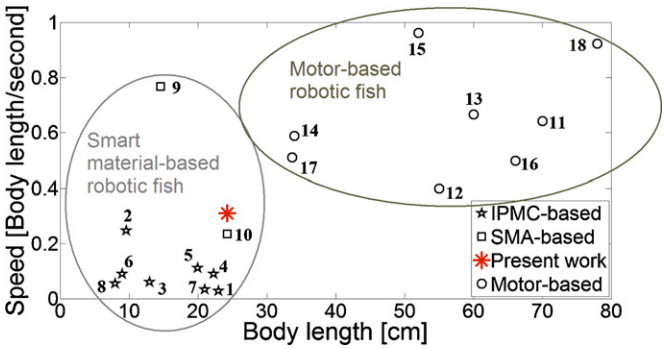

Figure 14. Performance comparison of smart material-based and motor-based untethered robotic fish (normalized swimming speed versus body length) showing the advantage of this work relative to other smart material-based untethered robotic fish in terms of the swimming speed and relative to the motor-based counterparts in terms of the body length.

Table 3. Performance comparison of smart material-based and motor-based untethered robotic fish based on the normalized swimming speed.

	Body length (cm)	Speed (cm s^{-1})	Body length/ Second
IPMC-based			
1 [22]	23	0.63	0.027
2 [18]	9.6	2.36	0.25
3 [28]	13	0.78	0.06
4 [27]	22.3	2	0.09
5 [24]	19.97	2.2	0.11
6 [29]	9	0.8	0.089
7 [30]	21	0.7	0.033
8 [31]	8	0.44	0.055
SMA-based			
9 [34]	14.6	11.2	0.77
10 [77]	24.3	5.7	0.23
MFC-based piezoelectric			
This work	24.26	7.5	**0.31**
Motor-based			
11 [78, 79]	70	45	0.64
12 [80]	55	22	0.40
13 [81]	60	40	0.67
14 [82]	34	20	0.59
15 [83, 84]	52	50	0.96
16 [85, 86]	66.1	33	0.50
17 [87]	33.7	17.2	0.51
18 [88, 89]	78	72	0.92

6. Conclusions

Bio-inspired aquatic robotics using macro-fiber composite (MFC) piezoelectric bimorphs is investigated theoretically and experimentally for fish-like locomotion. In-air and underwater dynamics of an MFC bimorph cantilever is modeled for small amplitude bending vibrations under piezoelectric actuation. Hydrodynamic effects are introduced to the electroelastic model based on Sader's work [57] on cantilevers vibrating in fluids for a wide range of Reynolds numbers. Underwater dynamics of the bimorph propulsor is coupled with Lighthill's elongated-body theory to predict the thrust output in quiescent water. In-air and underwater experiments are conducted for model validation and for the characterization of a bimorph propulsor. The hydrodynamic effects added to the electroelastic in-air model successfully predict the underwater dynamics for small oscillations. However, for future work, nonlinear electrohydroelastic modeling (combining nonlinear electroelastic dynamics [66–68] with nonlinear hydrodynamic effects [70, 71]) is required to predict the dynamics of the propulsor for arbitrary aspect ratios, relatively large oscillations, and under high electric field levels.

The underwater experiments resulted in mean thrust levels as high as 14 mN around 7 Hz for the peak-to-peak actuation voltage of 800 V using a 90 mm × 35 mm × 0.67 mm cantilever in the absence of a caudal fin extension (note that the MFCs can perform without depolarization up to peak-to-peak actuation voltage of 2000 V). Fish-like propulsors made of MFCs can therefore successfully imitate thrust levels of biological fish (see [90] for typical values). The dimensionless thrust coefficient is identified and the correlation between the mean thrust and modified Reynolds number is validated.

An untethered robotic fish prototype that incorporates a microcontroller and a printed-circuit-board (PCB) amplifier is developed and tested in free locomotion. A swimming speed of 0.3 body length per second (7.5 cm s^{-1} swimming speed for 24.3 cm body length at 5 Hz) is achieved for a non-optimized main body-propulsor combination. This swimming speed of the first prototype can be improved substantially by increasing the actuation voltage, optimizing the volume, and using a caudal fin extension. Following the performance comparison with the literature of untethered robotic fish, it is concluded that MFC-based robotic fish provides geometric scalability (as compared to motor-based robotic fish) and high performance swimming (as compared to IPMC-based robotic fish).

Acknowledgment

We would like to thank Martin Cacan for his assistance in CAD modeling and rapid prototyping of the robotic fish sample.

References

[1] Bandyopadhyay P R 2005 Trends in biorobotic autonomous undersea vehicles *IEEE J. Ocean. Eng.* **30** 109–39
[2] Roper D *et al* 2011 A review of developments towards biologically inspired propulsion systems for autonomous underwater vehicles *Proc. Inst. Mech. Eng. M* **225** 77–96
[3] Chu W S *et al* 2012 Review of biomimetic underwater robots using smart actuators *Int. J. Precis. Eng. Manuf.* **13** 1281–92
[4] Barrett D S 1994 The design of a flexible hull undersea vehicle propelled by an oscillator foil *MS Thesis* Department of Ocean Engineering, Massachusetts Institute of Technology, Boston, MA p 177
[5] Barrett D S 1996 Propulsive efficiency of a flexible hull underwater vehicle *PhD Thesis* Department of Ocean Engineering, Massachusetts Institute of Technology, Boston, MA p 215
[6] Anderson J M and Chhabra N K 2002 Maneuvering and stability performance of a robotic tuna *Integr. Comp. Biol.* **42** 118–26
[7] Low K and Willy A 2006 Biomimetic motion planning of an undulating robotic fish fin *J. Vib. Control* **12** 1337–59
[8] Valdivia y Alvarado P 2007 Design of biomimetic compliant devices for locomotion in liquid environments *PhD Thesis*

Department of Ocean Engineering, Massachusetts Institute of Technology, Boston, MA p 164

[9] Crespi A *et al* 2008 Controlling swimming and crawling in a fish robot using a central pattern generator *Auton. Robots* **25** 3–13

[10] Liu F, Lee K M and Yang C J 2012 Hydrodynamics of an undulating fin for a wave-like locomotion system design *IEEE/ASME Trans. Mechatronics* **17** 554–62

[11] Zhou C and Low K 2012 Design and locomotion control of a biomimetic underwater vehicle with fin propulsion *IEEE/ASME Trans. Mechatronics* **17** 25–35

[12] Wen L *et al* 2012 Quantitative thrust efficiency of a self-propulsive robotic fish: experimental method and hydrodynamic investigation *IEEE/ASME Trans. Mechatronics* **99** 1–12

[13] Serchi F G, Arienti A and Laschi C 2012 Biomimetic vortex propulsion: toward the new paradigm of soft unmanned underwater vehicles *IEEE/ASME Trans. Mechatronics* **99** 1–10

[14] Shahinpoor M 1992 Conceptual design, kinematics and dynamics of swimming robotic structures using ionic polymeric gel muscles *Smart Mater. Struct.* **1** 91–95

[15] Mojarrad M and Shahinpoor M 1996 Noiseless propulsion for swimming robotic structures using polyelectrolyte ion-exchange membrane *Proc. SPIE* **2716** 183–92

[16] Laurent G and Piat E 2001 Efficiency of swimming microrobots using ionic polymer metal composite actuators *Proc. IEEE Int. Conf. on Robotics and Automation* vol 4 pp 3914–9

[17] Kim K J 2003 Fabrication and development of electroactive ionic polymer–metal composites and their applications as smart materials *THERMEC '2003* vols 426–32 pp 2249–54

[18] Kim B *et al* 2005 A biomimetic undulatory tadpole robot using ionic polymer–metal composite actuators *Smart Mater. Struct.* **14** 1579–85

[19] Chung C K *et al* 2005 A novel fabrication of ionic polymer–metal composites (IPMC) actuator with silver nano-powders *Transducers '05: Digest of Technical Papers* vols 1 and 2 pp 217–20

[20] Guo S X *et al* 2006 Underwater swimming micro robot using IPMC actuator *ICMA 2006: Proc. IEEE Int. Conf. on Mechatronics and Automation* vols 1–3 pp 249–54

[21] Chung C K *et al* 2006 A novel fabrication of ionic polymer–metal composites (IPMC) actuator with silver nano-powders *Sensors Actuators* B **117** 367–75

[22] Tan X B *et al* 2006 An autonomous robotic fish for mobile sensing *IEEE/RSJ Int. Conf. on Intelligent Robots and Systems* vols 1–12 pp 5424–9

[23] Brunetto P *et al* 2008 A model of ionic polymer–metal composite actuators in underwater operations *Smart Mater. Struct.* **17** 025029

[24] Mbemmo E *et al* 2008 Modeling of biomimetic robotic fish propelled by an ionic polymer–metal composite actuator *IEEE Int. Conf. on Robotics and Automation* vols 1–9 pp 689–94

[25] Jeon J H, Yeorn S W and Oh I K 2008 Fabrication and actuation of ionic polymer metal composites patterned by combining electroplating with electroless plating *Composites* A **39** 588–96

[26] de Witt B J and Hugo R J 2009 A preliminary study of the transition of an in-line pipe vortex to slug flow using particle image velocimetry *Proc. ASME Fluids Engineering Division Summer Conf. (2008)* vol 1 Pts A and B pp 637–46

[27] Chen Z, Shatara S and Tan X B 2010 Modeling of biomimetic robotic fish propelled by an ionic polymer-metal composite caudal fin *IEEE/ASME Trans. Mechatronics* **15** 448–59

[28] Aureli M, Kopman V and Porfiri M 2010 Free-locomotion of underwater vehicles actuated by ionic polymer metal composites *IEEE/ASME Trans. Mechatronics* **15** 603–14

[29] Takagi K *et al* 2006 Development of a Rajiform swimming robot using ionic polymer artificial muscles *IEEE/RSJ Int. Conf. on Intelligent Robots and Systems* vols 1–12 pp 1861–6

[30] Chen Z, Um T I and Zhu J 2011 Bio-inspired robotic Cownose ray propelled by electroactive polymer pectoral fin *Proc. ASME Int. Mechanical Engineering Congress and Exposition* pp 817–24

[31] Chen Z, Um T I and Bart-Smith H 2011 Ionic polymer–metal composite enabled robotic manta ray *Proc. SPIE* **7976** 797637

[32] Shinjo N and Swain G W 2004 Use of a shape memory alloy for the design of an oscillatory propulsion system *IEEE J. Ocean. Eng.* **29** 750–5

[33] Wang Z L *et al* 2008 A micro-robot fish with embedded SMA wire actuated flexible biomimetic fin *Sensors Actuators* A **144** 354–60

[34] Wang Z *et al* 2008 Embedded SMA wire actuated biomimetic fin: a module for biomimetic underwater propulsion *Smart Mater. Struct.* **17** 025039

[35] Cho K J *et al* 2008 Design, fabrication and analysis of a body-caudal fin propulsion system for a microrobotic fish *IEEE Int. Conf. on Robotics and Automation* vols 1–9 pp 706–11

[36] Rossi C *et al* 2011 Bending continuous structures with SMAs: a novel robotic fish design *Bioinspir. Biomim.* **6** 045005

[37] Rossi C *et al* 2011 A motor-less and gear-less bio-mimetic robotic fish design *IEEE Int. Conf. on Robotics and Automation* pp 3646–51

[38] Zhang Y S and Liu G J 2005 Design, analysis and experiments of a wireless swimming micro robot *IEEE Int. Conf. on Mechatronics and Automations* vol 2 pp 946–51

[39] Zhang Y S and Liu G J 2005 Wireless micro biomimetic swimming robot based on giant magnetostrictive films *IEEE Int. Conf. on Robotics and Biomimetics* pp 195–200

[40] Zhang Y S and Liu G J 2009 Wireless swimming microrobot: design, analysis, and experiments *Trans. ASME, J. Dyn. Syst. Meas. Control* **131** 011004

[41] Zhang Z 2007 Design and control of a fish-like robot using an electrostatic motor *Proc. IEEE Int. Conf. on Robotics and Automation (ROME)* pp 974–9

[42] Zhang Z, Philen M and Neu W 2010 A biologically inspired artificial fish using flexible matrix composite actuators: analysis and experiment *Smart Mater. Struct.* **19** 094017

[43] Philen M and Neu W 2011 Hydrodynamic analysis, performance assessment, and actuator design of a flexible tail propulsor in an artificial alligator *Smart Mater. Struct.* **20** 094015

[44] Uchino K 2008 Piezoelectric actuators 2006—expansion from IT/robotics to ecological energy applications *J. Electroceram.* **20** 301–11

[45] Cook-Chennault K A, Thambi N and Sastry A M 2008 Powering MEMS portable devices—a review of non-regenerative and regenerative power supply systems with special emphasis on piezoelectric energy harvesting systems *Smart Mater. Struct.* **17** 043001

[46] Trolier-McKinstry S and Muralt P 2004 Thin film piezoelectrics for MEMS *J. Electroceram.* **12** 7–17

[47] Erturk A and Delporte G 2011 Underwater thrust and power generation using flexible piezoelectric composites: an experimental investigation toward self-powered swimmer-sensor platforms *Smart Mater. Struct.* **20** 125013

[48] Erturk A and Inman D J 2011 *Piezoelectric Energy Harvesting* (Chichester: Wiley) p 392

[49] Wilkie W K *et al* 2000 Low-cost piezocomposite actuator for structural control applications *Proc. SPIE* **3991** 323
[50] High J W and Wilkie W K 2003 Method of fabricating NASA-standard macro-fiber composite piezoelectric actuators *Technical Report* NASA/TM-2003-2 12427, ARL-TR-2833, Langley Research Center, National Aeronautics and Space Administration, Hampton, VA
[51] Bryant R G 2007 Overview of NASA Langley's piezoelectric ceramic packaging technology and applications Langley Research Center, National Aeronautics and Space Administration, Hampton, VA
[52] Fukuda T *et al* 1995 Steering mechanism and swimming experiment of micro mobile robot in water *IEEE Proc. Micro Electro Mechanical Systems* pp 300–5
[53] Heo S *et al* 2007 Effect of an artificial caudal fin on the performance of a biomimetic fish robot propelled by piezoelectric actuators *J. Bionic Eng.* **4** 151–8
[54] Wiguna T *et al* 2009 Design and experimental parameteric study of a fish robot actuated by piezoelectric actuators *J. Intell. Mater. Syst. Struct.* **20** 751–8
[55] Ming A G *et al* 2009 Development of underwater robots using piezoelectric fiber composite *IEEE Int. Conf. on Robotics and Automation* vols 1–7 pp 3435–40
[56] Sfakiotakis M, Lane D M and Davies J B C 1999 Review of fish swimming modes for aquatic locomotion *IEEE J. Ocean. Eng.* **24** 237–52
[57] Sader J E 1998 Frequency response of cantilever beams immersed in viscous fluids with applications to the atomic force microscope *J. Appl. Phys.* **84** 64–76
[58] Van Eysden C A and Sader J E 2007 Frequency response of cantilever beams immersed in viscous fluids with applications to the atomic force microscope: arbitrary mode order *J. Appl. Phys.* **101** 044908
[59] Chon J W M, Mulvaney P and Sader J E 2000 Experimental validation of theoretical models for the frequency response of atomic force microscope cantilever beams immersed in fluids *J. Appl. Phys.* **87** 3978–88
[60] Van Eysden C A and Sader J E 2006 Resonant frequencies of a rectangular cantilever beam immersed in a fluid *J. Appl. Phys.* **100** 114916
[61] Lighthill M J 1960 Note on the swimming of slender fish *J. Fluid Mech.* **9** 305–17
[62] Lighthill M J 1969 Hydromechanics of aquatic animal propulsion *Annu. Rev. Fluid Mech.* **1** 413–446
[63] Lighthill M J 1970 Aquatic animal propulsion of high hydromechanical efficiency *J. Fluid Mech.* **44** 265–301
[64] Lighthill M J 1971 Large-amplitude elongated-body theory of fish locomotion *Proc. R. Soc. Lond.* B **179** 125–38
[65] Meirovitch L 2001 *Fundamentals of Vibrations* (Boston: McGraw-Hill) 806 pp
[66] Wolf K and Gottlieb O 2002 Nonlinear dynamics of a noncontacting atomic force microscope cantilever actuated by a piezoelectric layer *J. Appl. Phys.* **91** 4701–9
[67] Usher T and Sim A 2005 Nonlinear dynamics of piezoelectric high displacement actuators in cantilever mode *J. Appl. Phys.* **98** 064102
[68] Stanton S C *et al* 2010 Nonlinear piezoelectricity in electroelastic energy harvesters: modeling and experimental identification *J. Appl. Phys.* **108** 074903
[69] Maali A *et al* 2005 Hydrodynamics of oscillating atomic force microscopy cantilevers in viscous fluids *J. Appl. Phys.* **97** 074907
[70] Aureli M, Basaran M E and Porfiri M 2012 Nonlinear finite amplitude vibrations of sharp-edged beams in viscous fluids *J. Sound Vib.* **331** 1624–654
[71] Aureli M and Porfiri M 2010 Low frequency and large amplitude oscillations of cantilevers in viscous fluids *Appl. Phys. Lett.* **96** 164102
[72] Chu W 1963 *Technical Report* No 2 DTMB, Contract NObs-86396 (X), Southwest Research Institute, San Antonio, TX
[73] Taylor G 1951 Analysis of the swimming of microscopic organisms *Proc. R. Soc. Lond.* B **139** 141
[74] Taylor G 1952 The action of waving cylindrical tails in propelling microscopic organisms *Proc. R. Soc. Lond.* A **211** 225–39
[75] Anton S R, Erturk A and Inman D J 2010 Multifunctional self-charging structures using piezoceramics and thin-film batteries *Smart Mater. Struct.* **19** 115021
[76] Abdelnour K *et al* 2009 Hydrodynamics of underwater propulsors based on ionic polymer–metal composites: a numerical study *Smart Mater. Struct.* **18** 085006
[77] Wang Z L *et al* 2009 A micro biomimetic manta ray robot fish actuated by SMA *IEEE Int. Conf. on Robotics and Biomimetics* vols 1–4 pp 1809–13
[78] Wang W B *et al* 2009 Bio-inspired design and realization of a novel multimode amphibious robot *IEEE Int. Conf. on Automation and Logistics* vols 1–3 pp 140–5
[79] Ding R *et al* 2009 CPG-based dynamics modeling and simulation for a biomimetic amphibious robot *IEEE Int. Conf. on Robotics and Biomimetics* vols 1–4 pp 1657–62
[80] Fan R F *et al* 2005 Optimized design and implementation of biomimetic robotic dolphin *IEEE Int. Conf. on Robotics and Biomimetics* pp 484–9
[81] Hirata K 2000 Development of experimental fish robot *Proc. ISME Tokyo* vol 2 pp 711–4
[82] Hirata K, Takimoto T and Tamura K 2000 Study on turning performance of a fish robot *Proc. 1st Int. Symp. on Aqua Bio-Mechanisms*
[83] Liu J-D and Hu H 2006 Biologically inspired behaviour design for autonomous robotic fish *Int. J. Autom. Comput.* **3** 336–47
[84] Hu H 2006 Biologically inspired design of autonomous robotic fish at Essex *IEEE SMC UK-RI Chapter Conf.* pp 3–8
[85] Low K 2011 Current and future trends of biologically inspired underwater vehicles *Proc. Defense Science Research Conf. and Expo* 6026887
[86] Low K H and Chong C W 2010 Parametric study of the swimming performance of a fish robot propelled by a flexible caudal fin *Bioinspir. Biomim.* **5** 046002
[87] Papadopoulos E, Apostolopoulos E and Tsigkourakos P 2009 Design, control, and experimental performance of a teleoperated robotic fish *MED '09:17th Mediterranean Conf. on Control and Automation* vols 1–3 pp 766–71
[88] Shin D, Na S Y, Kim J Y and Baek S J 2007 Fish robots for water pollution monitoring using ubiquitous sensor networks with sonar localization *Int. Conf. on Convergence Information Technology* pp 1298–303
[89] Shin D *et al* 2008 Fuzzy neural networks for obstacle pattern recognition and collision avoidance of fish robots *Soft Comput.* **12** 715–20
[90] Lauder G V and Drucker E G 2002 Forces, fishes, and fluids: hydrodynamic mechanisms of aquatic locomotion *News Physiol. Sci.* **17** 235–40